

Article

Crystallization of Poly(ethylene oxide)-Based Triblock Copolymers in Films Swollen-Rich in Solvent Vapors

Iulia Babutan ^{1,2}, Otto Todor-Boer ³ , Leonard Ionut Atanase ^{4,5} , Adriana Vulpoi ¹ and Ioan Botiz ^{1,2,*}

¹ Interdisciplinary Research Institute on Bio-Nano-Sciences, Babeş-Bolyai University, 400271 Cluj-Napoca, Romania; iulia.babutan@ubbcluj.ro (I.B.); adriana.vulpoi@ubbcluj.ro (A.V.)

² Faculty of Physics, Babeş-Bolyai University, 400084 Cluj-Napoca, Romania

³ INCDO-INOE 2000, Research Institute for Analytical Instrumentation, 400293 Cluj-Napoca, Romania; otto.todor@icia.ro

⁴ Department of Biomaterials, Faculty of Medical Dentistry, “Apollonia” University of Iasi, 700511 Iasi, Romania; leonard.atanase@univapollonia.ro

⁵ Academy of Romanian Scientists, 050045 Bucharest, Romania

* Correspondence: ioan.botiz@ubbcluj.ro

Abstract: In this study, we employed a polymer processing method based on solvent vapor annealing in a confined environment to swell-rich thin films of polybutadiene-*b*-poly(2-vinylpyridine)-*b*-poly(ethylene oxide) triblock copolymers and to promote their crystallization. As revealed by optical and atomic force microscopy, thin films of triblock copolymers containing a rather short crystalline poly(ethylene oxide) block that was massively obstructed by the other two blocks were unable to crystallize following the spin-casting process, and their further swelling in solvent vapors was necessary in order to produce polymeric crystals displaying a dendritic morphology. In comparison, thin films of triblock copolymers containing a much longer poly(ethylene oxide) block that was less obstructed by the other two blocks were shown to crystallize into dendritic structures right after the spin-casting procedure, as well as upon rich swelling in solvent vapors.

Keywords: block copolymers; thin films; solvent vapor annealing; polymer crystallization; atomic force microscopy



Citation: Babutan, I.; Todor-Boer, O.; Atanase, L.I.; Vulpoi, A.; Botiz, I.

Crystallization of Poly(ethylene oxide)-Based Triblock Copolymers in Films Swollen-Rich in Solvent Vapors. *Coatings* **2023**, *13*, 918. <https://doi.org/10.3390/coatings13050918>

Academic Editors: Mohor Mihelčić and Ajay Vikram Singh

Received: 27 April 2023

Revised: 8 May 2023

Accepted: 11 May 2023

Published: 14 May 2023



Copyright: © 2023 by the authors. Licensee MDPI, Basel, Switzerland. This article is an open access article distributed under the terms and conditions of the Creative Commons Attribution (CC BY) license (<https://creativecommons.org/licenses/by/4.0/>).

1. Introduction

The wide diversity of polymeric properties has its first source in the nature of polymers' soft material component units named monomers [1–11]. The capability of long polymer chains to adopt, after specific processing conditions, a multitude of conformational arrangements at multiple length scales, represents a second consistent source that nourishes the development of new and/or enhanced polymer properties in thin films and on various surfaces of interest, in solutions and in the solid state [2,9,12–16]. Obviously, the optimized polymer properties can be advantageously employed to design and produce various functional devices, develop new technologies, and engineer high-impact applications [7,17–27].

There is a broad range of prominent processing methods that can efficiently alter the microstructure of various polymer chains and tune their molecular arrangements at micrometer and nanometer scales [10,14,28–34]. Such methods can be used to align polymer molecules in thin films during [35–37] or after [15,33,38–43] their fabrication, as well as in solutions [44–46] and in the solid state [14,47,48], and may include the selection of solvent quality [49] and polymer concentration [50], addition of non-solvents [51], employment of convective forces [31,34], thermal annealing [40], pressure [52] or mechanical stretching [53], and use of space confinements [54,55] or annealing in solvent vapors [39,41]. The aforementioned methods mainly rely on physical processes such as self-assembly [56–58] or crystallization [40,41,59–62]. In particular, the crystallization process becomes important

when employed to control the mechanical [63,64], optoelectronic [64,65] or other [64,66] properties of polymeric materials. Interestingly, while the confinement of polymer chains has been reported to exhibit significant impact on the kinetics of crystallization [67] of block copolymers (BCPs), the solvent vapor annealing procedure has proved to be critical in the ordering of a large variety of BCPs [68–70] inclusively when investigating highly complex molecules [39].

In this study, we relied on a processing approach that takes advantage of both confinement and solvent vapor annealing (C-SVA) and further induces crystallization of BCP systems based on rather short crystallizable poly(ethylene oxide) (PEO) blocks. The PEO blocks are composed of only about 104 and 154 monomer units, with their corresponding number average molecular weights being determined as $M_{n\text{PEO}104} = 4600$ g/mol and $M_{n\text{PEO}154} = 6800$ g/mol, respectively [71]. We show that although the aforementioned blocks are capable of crystallizing at temperatures below 40 °C [72], triblock copolymers based on such blocks will not crystallize into large dendritic crystals under spin-casting conditions, unless further processed by utilizing the improved C-SVA approach [73,74] (note that polymer chains containing much larger numbers of ethylene oxide monomers are known to crystallize following spin casting or thermal annealing processes at room temperature or various higher crystallization temperatures; such macromolecules are often used as model systems for studying general concepts of the crystallization process [38,75]). Compared to other SVA-based studies [39,41,42], this improved approach was recently shown to be capable of self-assembling various BCP systems into highly ordered nanostructures [73,74]. It consists of a sample chamber of reduced depth and well-regulated temperature and a “bubbling” system able to inject precise amounts of solvent vapors inside the sample chamber (Figure 1). With this design, the rich-swelling of BCP films is possible without encountering weak variations in the sample temperature during the swelling-deswelling processes, and thus without experiencing unwanted fluctuations in the swollen-film thickness that can generate film defects upon drying [73].

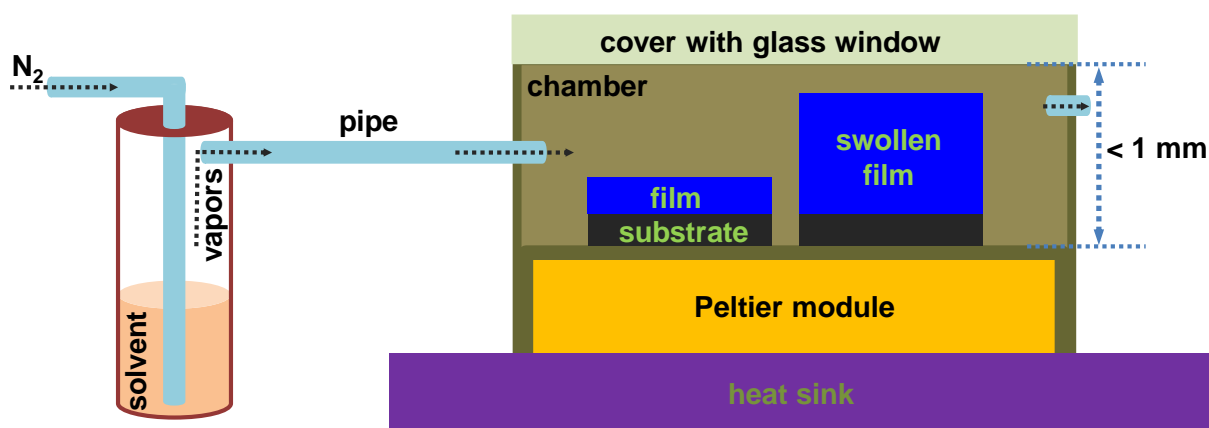


Figure 1. Schematic representation of the experimental setup used to process thin BCP films. In this setup, the Peltier module was connected both to a temperature controller and a PT100 sensor. Meanwhile, the heat sink was coupled to a fan. At the same time, the pipe transporting solvent vapors was connected to a nitrogen-based “bubbling” system depicted on the left. The scheme shows both the unswollen (on the left) and swollen (on the right) states of a BCP film. Note that the dimensions are not drawn at scale.

2. Materials and Methods

The polymer system employed in this study was a polybutadiene-*b*-poly(2-vinylpyridine)-*b*-poly(ethylene oxide) (PB-*b*-P2VP-*b*-PEO) triblock copolymer (see its chemical structure depicted in Figure 2). We employed four different BCP systems displaying number average molecular weights of $M_n = 20,500$ g/mol (PB₁₀₀-*b*-P2VP₁₀₀-*b*-PEO₁₀₄), $M_n = 28,200$ g/mol (PB₁₈₅-*b*-P2VP₁₀₈-*b*-PEO₁₅₄), $M_n = 76,000$ g/mol (PB₃₄₈-*b*-P2VP₂₅₂-

b-PEO₆₉₇) and $M_n = 26,400$ g/mol (PB₆₆-*b*-P2VP₆₉-*b*-PEO₃₅₆), respectively [71]. These polymer systems were synthesized by living anionic polymerization in tetrahydrofuran (THF) in the presence of cumyl potassium (PIK) as initiator, and through the employment of well-established procedures [71,76,77].

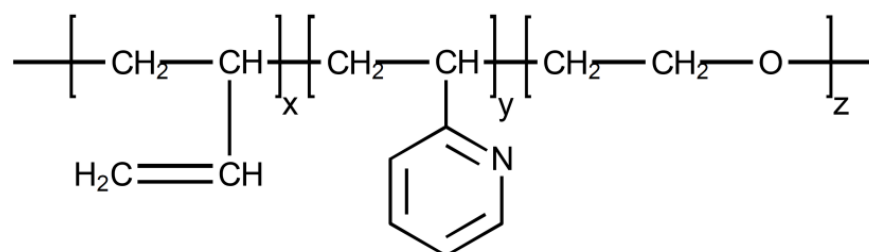


Figure 2. Chemical structure of the PB_x-*b*-P2VP_y-*b*-PEO_z triblock copolymer employed in this study. Here, x, y and z are the degrees of polymerization corresponding to each of the three blocks (x is representing the values of 66, 100, 185 and 348, y is representing the values of 69, 100, 108 and 252, and z is representing the values of 356, 104, 154 and 697, respectively).

The reagent used for the preparation of copolymer solutions was toluene (98%), purchased from the Chemical Company (Iasi, Romania). Toluene was employed because it is a good solvent for both PEO and PB. Copolymer solutions were prepared by dissolving 10 mg of copolymer powder in 1 mL of toluene. The process was followed by gentle stirring to further stimulate dissolution and homogenization. Afterwards, polymeric solutions were annealed at 70 °C in a silicon oil bath (ONE 7-45, Schwabach, Germany) for 30 min to complete the dissolution of copolymers in toluene.

Thin triblock copolymer films of a thickness of 79 ± 5 nm (this value was determined after scratching a film and measuring the corresponding height profile with the atomic force microscopy/AFM) were obtained by spin casting copolymer solutions onto solid silicon substrates using a WS-650mz23nppb spin coater from Laurell Technologies Corporation (North Wales, PA, USA). Films were deposited at a speed of 2000 rpm for 30 s. Type 4PO/5-10/380 \pm 15/SSP/TTV < 5 silicon substrates were acquired from Siebert Wafer GmbH (Aachen, Germany) and were subjected to UV-ozone treatment for 20 min (in a PSD Pro Series-Digital UV Ozone System from Novascan; Boone, IA, USA) before their further use.

For the swelling and deswelling of BCP films via their exposure to toluene vapors in a quasi-confined environment (C-SVA), we have used a home-made equipment consisting of an aluminum chamber with a high-performance Peltier element (15.4 V/8.5 A from Stonecold) placed beneath (see Figure 1). The 100 W powerful Peltier module permitted the setup to exhibit a maximum temperature difference ΔT between the two sides of about 58 °C. The temperature of the Peltier module (i.e., the temperature of the bottom of the sample chamber and thus, the temperature of the film; note that the bottom of the chamber was thermally separated from the rest of the chamber by design) could be regulated by a temperature controller (model TCM U 10 A from Electron Dynamics Ltd.; Southampton, UK) that received feedback from a PT100 temperature sensor located in the chamber, in the vicinity of the BCP film. The PT100 sensor was continuously communicating the film temperature to the controller. The latter could change the strength and direction of the electric current depending on whether it needed to cool or heat the system (electricity was provided by a 12 V/10 A power supply). Moreover, an aluminum heat sink and a fan were placed on the other side of the Peltier module, which helped to equalize the ΔT temperature. The controller was connected to computer software that used proportional integral derivative technology to accurately set the temperature within the desired time. With the above-described device, it was possible to control the sample temperature with a precision of 0.01 °C and to keep it constant over time. Furthermore, the time required to reach a specific temperature could be varied within the seconds–hours range. This allowed

us to finely tune the rate at which the temperature changed and to avoid weak variations in the sample temperature, which may appear when reaching a specific temperature setpoint during a swelling or deswelling procedure. Finally, note that the sample chamber was saturated with toluene vapors using a nitrogen-based “bubbling” system that was connected to a flow meter that allowed the amount of vapors to be regulated.

The following experimental procedure was used to swell/de-swell thin BCP films in a quasi-confined environment saturated with toluene vapors. A PB-*b*-P2VP-*b*-PEO triblock copolymer film was placed in the sample chamber. While the chamber was heated up to 40 °C, the desired quantity of toluene vapors was bubbled inside. Next, the film temperature was set to 15 °C. While the temperature was decreasing at a rate of 0.3 °C/s, at around 22 °C the toluene vapors started to condense gradually on the surface of the film and the latter started to swell and change its color. This change in the interference colors was associated with the changes in the film thickness and could be used to monitor the thickness of the latter in its swollen state (an interference color–film thickness calibration can be generated before the start of the swelling experiments by measuring the thickness of many BCP films using the AFM technique and then associating each thickness to the corresponding film color observed under the optical microscope; see additional details on the procedure elsewhere [39,41,78]). At 15 °C there were enough toluene vapors condensed on the film to transform it into a quasi-two-dimensional (2D) “solution” with a polymer concentration (c_p) of about 7% \pm 3% (this concentration value was calculated as the ratio between the initial film thickness and the thickness of the swollen film; see details in [39,41,78]). After about 30 s at this low c_p , we reversed the process and initiated the deswelling process when the film temperature was increased slowly back to 40 °C, at a rate of only 0.01 °C/s. During this time, toluene vapors began to gradually evaporate and the film slowly returned to its original thickness, but with its surfaces covered with newly induced crystalline structures.

For the acquisition of AFM images, a system from Molecular Devices and Tools for Nano Technology (NT-MDT) mounted on an Olympus IX71 optical microscope was used in noncontact (tapping) mode. The AFM measurements were conducted utilizing high resolution Noncontact Golden Silicon probes from NT-MDT. These probes had a tip radius of curvature smaller than 10 nm and a tip height in the range of 14–16 μm . Moreover, they were coated with Au on the detector side cantilever. The latter had a length of 125 \pm 5 μm , and displayed a resonance frequency in the range of 187–230 kHz and a nominal force constant ranging between 1.45–15.1 N/m. The AFM images (256 \times 256 lines) were obtained using a scanning speed of about 1–2 $\mu\text{m/s}$ and a setpoint ranging between 9 and 12 V. The setpoint was adjusted so that a very soft tapping regime was obtained. The optical microscopy micrographs were acquired using a KERN OKN-177 optical microscope operating in reflection mode.

3. Results and Discussion

The main objective of this study was to reveal the impact of C-SVA processing on the crystallization of thin BCP films. To achieve this objective, we firstly used a triblock PB₁₀₀-*b*-P2VP₁₀₀-*b*-PEO₁₀₄ copolymer system containing one crystalline [40] PEO block. Because the PEO block was rather short (it comprised only 104 repeating monomers) and comparable to the lengths of the other two constituent PB and P2VP blocks (each containing 100 corresponding monomers), we expected that this triblock copolymer would face difficulties in crystallizing (i.e., to nucleate and grow into single crystals) due to unavoidable obstructions exerted by the non-crystalline blocks. Indeed, many attempts to nucleate and crystallize thin PB₁₀₀-*b*-P2VP₁₀₀-*b*-PEO₁₀₄ films from the melt at various temperatures below 40 °C were unsuccessful (although partial melting of such films was observable under the optical microscope at 67 °C and above, the subsequent crystallization in the temperature range of 26–38 °C would not occur, possibly due to insufficiently increased chain mobility combined with the inhibitions generated by the non-crystalline blocks). Moreover, crystallization would also be difficult under normal, high-speed spin-

casting conditions that would kinetically trap the films in a rather disordered state, as there is only limited time for the BCP to initiate nucleation and subsequent crystallization prior to the loss of solvent. This latter statement was confirmed by the results presented in Figure 3. As we can observe in the optical micrograph in Figure 3b, there were no crystals forming during and/or after the spin-casting process, besides some irregular and randomly distributed elongated objects (of a length of 10–20 μm , as indicated by the yellow dotted arrows; a part of such a quasi-flat object was further indicated by the dotted shape in Figure 3d). The AFM height images presented in Figure 3d,f further demonstrated that the rest of the film surface was covered with bright-colored domains a few tens of nanometers tall, surrounding some “empty” and dark-colored irregular regions. Nonetheless, these latter regions appeared brighter in the AFM phase image in Figure 3h, indicating that at the bottom they were made of rather stiffer structures, possibly some poorly developed aggregates or crystalline objects. Instead, the taller bright-colored domains visible in Figure 3f were composed of a rather soft, amorphous material, as indicated by their darker appearance in the AFM phase image (Figure 3h). Here, some rather circular sub-50 nm nanostructures, emphasized in Figure 3j by the dotted circular shapes, could nonetheless be observed.

In comparison, the as-cast $\text{PB}_{100}\text{-}b\text{-P2VP}_{100}\text{-}b\text{-PEO}_{104}$ BCP film that was further processed with the C-SVA method exhibited a morphology composed of essentially single crystals randomly distributed over the whole surface and displaying a dendritic structure (Figures 3a,c and 4a). This observation proved that processing with the C-SVA method favored and induced crystallization, even though the crystalline PEO block was short and well obstructed by the other two blocks and otherwise did not form crystals. Moreover, the dendritic crystals shown in Figure 4a nucleated and grew during the C-SVA processing, within the range of 17–20 $^{\circ}\text{C}$ while the c_p was determined to increase from about 20% to around 40% (note that the four crystals numbered in their centers are “deformed” due to their partial coalescence).

All the above experimental observations suggested that dendritic crystals only formed when polymer chains experienced high mobilities conferred by the rather diluted quasi-2D “film-solution” regime. This was not the case during the thermal annealing, when chain mobilities are expected to be lower than those in solutions or during the spin-casting process, when such mobilities are rapidly decreasing with the dramatic evaporation of the solvent. Clearly, the dendritic crystals are a result of (partial) alignments of, at least, PEO molecular chains (i.e., their crystallization). The growth of these crystals was driven not only by the transport of the molecules to the crystal (which is ultimately dictated by the concentration of polymer molecules in rich-swollen “film-solutions” and most probably by their diffusion rate [75]), but also by the probability of a polymer chain attaching to the surface of a crystal. Considering that the dendritic crystals formed in about 5 min (while increasing the sample temperature from about 17 $^{\circ}\text{C}$ to 20 $^{\circ}\text{C}$, with a rate of 0.01 $^{\circ}\text{C}/\text{s}$) in a regime where the molecules most likely experienced high mobilities that favored the diffusion of molecules, we tentatively conclude that the corresponding attachment probability was rather high and most probably dominated by the diffusion-limited aggregation that finally led to a dendritic morphology [75].

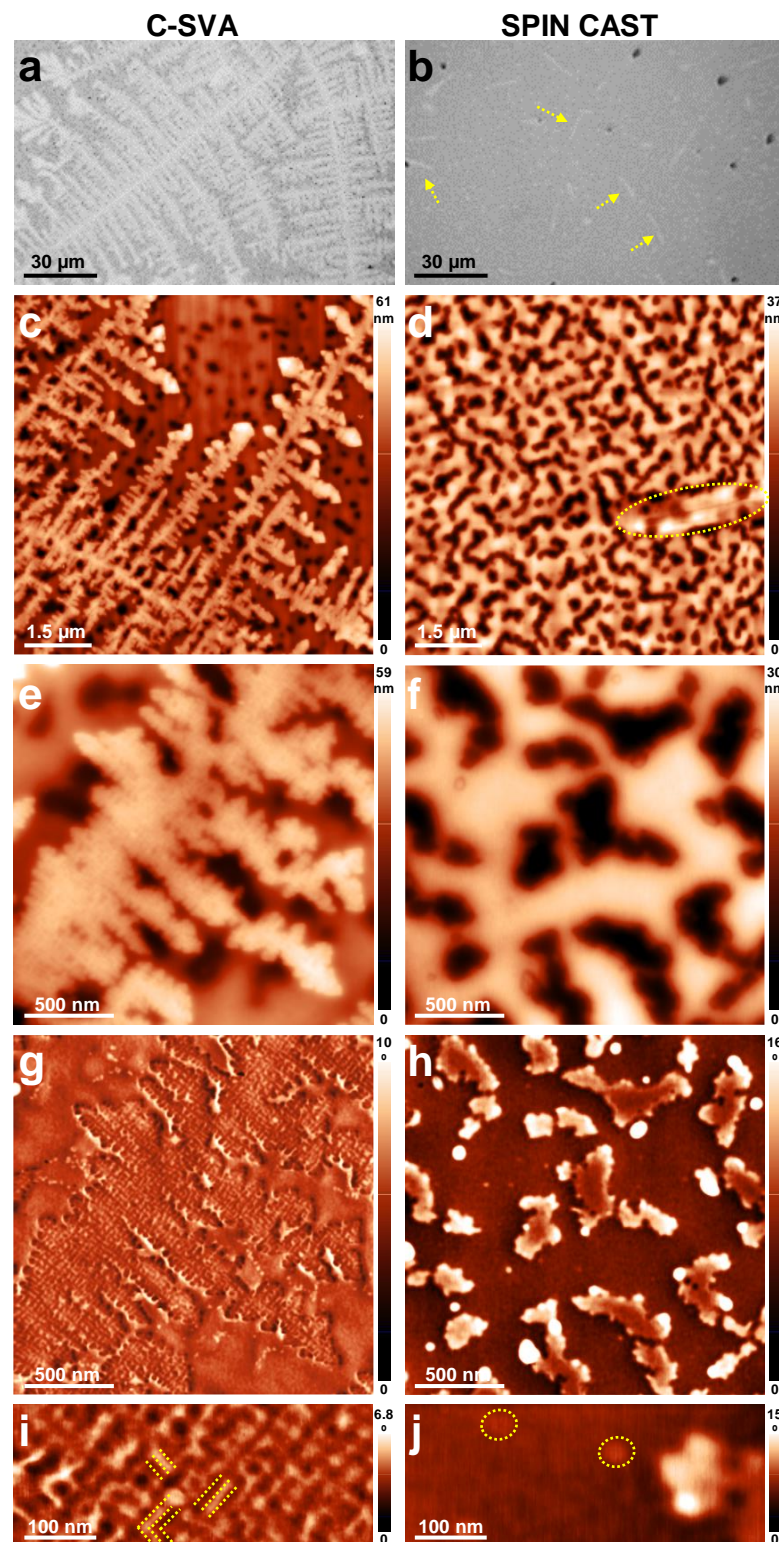


Figure 3. Optical micrographs (a,b) and AFM height (c–f) and phase (g–j) images depicting the surface microstructure observed in a thin film of PB₁₀₀-*b*-P2VP₁₀₀-*b*-PEO₁₀₄ after (a,c,e,g,i) and before (b,d,f,h,j) its exposure to toluene vapors in a rather confined sample chamber. While height (e) and phase (g) images each represent a zoom-in of a region depicted in (c), images in (f,h) correspond to a zoom-in of a region shown in (d). Moreover, images presented in (i,j) are each a zoom-in of the images portrayed in (g,h), respectively. The only purpose of the dotted arrows, shapes and lines is to guide the eye.

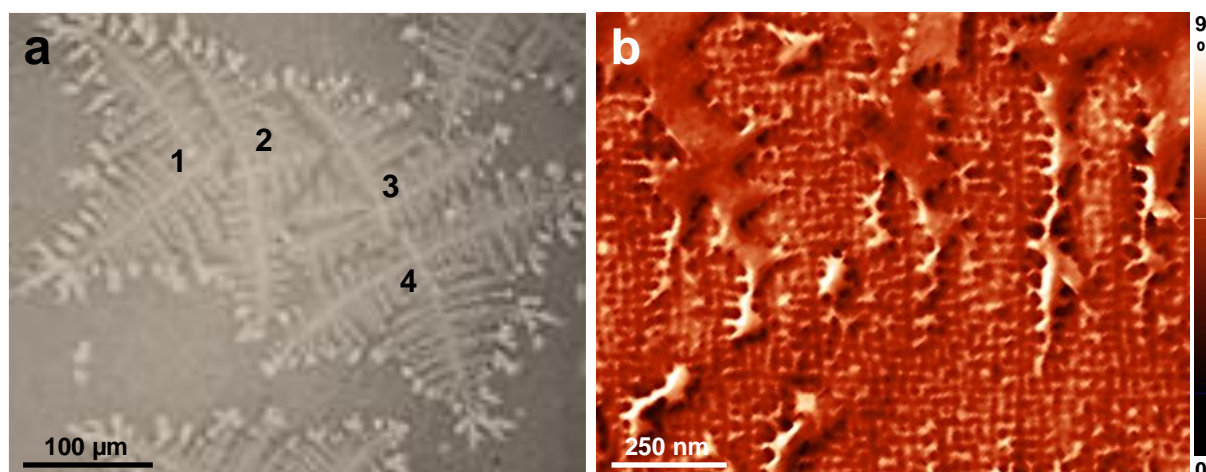


Figure 4. (a) Four (partially) coalesced single crystals of dendritic structures observed under the optical microscope in a PB_{100} - b - $P2VP_{100}$ - b - PEO_{104} thin film after its rich-exposure to toluene vapors. (b) Zoom-in and a 230° rotation of the AFM phase micrograph shown in Figure 3g realized in order to better emphasize the existence of 16 ± 2 nm large substructures.

Furthermore, the average thickness of the dendritic crystal presented in Figure 3c,e was extracted from multiple AFM cross-section profiles and was estimated to be 26 ± 5 nm. This value seemed to match the thickness of a PEO crystalline lamella, if considering that the maximum length of a crystalline PEO chain in its fully extended conformation is almost 29 nm (according to the literature, the dimension of one ethylene oxide monomer is 0.2783 nm [79]). Nonetheless, we do not know whether the crystal extended deeper within the 79 nm thick film, below the surface probed by the AFM. Additionally, the semicrystalline P2VP block could possibly extend the lamellar thickness by another 25 nm (100×0.25 nm [80,81]). Therefore, it is not possible to conclude whether the observed crystals were made of folded, tilted or fully extended chains without a further structural analysis employing X-ray experiments. Nonetheless, by comparing the crystal with its surrounding areas in the AFM phase image shown in Figure 3g, we observed that the color of the crystalline regions appeared to be slightly lighter than that of the surrounding areas, pointing towards a stiffer material. This was in accordance with the expectation that a crystalline material should be stiffer than its uncrystallized counterpart. A further analysis on the crystal morphology revealed not only that the dendritic crystals were composed, as expected, of a multitude of orthogonal branches, but also that these branches exhibited fine, rather orthogonal substructures of a lateral dimension of 16 ± 2 nm (see the dotted lines in the AFM image of Figure 3i and the high magnification of substructures in Figure 4b). To correlate this value with the dimension of the polymer chains and their precise arrangements within the crystal, a full structural analysis based on X-ray measurements will be needed in the future.

In order to further demonstrate that the C-SVA approach can efficiently induce and promote the crystallization process even under unfavorable conditions (i.e., when the PEO block is well obstructed by the other two blocks), we have further increased the length of all blocks, while maintaining a similar ratio between the number of ethylene oxide monomers and the number of total butadiene and 2-vinylpyridine monomers (~ 0.52). In this case, the resulting PB_{185} - b - $P2VP_{108}$ - b - PEO_{154} BCP system possessed a longer PEO crystalline chain, but was still well obstructed by the other two blocks. Figure 5 shows structures obtained in a PB_{185} - b - $P2VP_{108}$ - b - PEO_{154} film after and before its processing in toluene vapors. While the optical micrograph presented in Figure 5a and corresponding to the processed film clearly emphasized the presence of crystals of a seaweed dendritic morphology [82,83] with growing tips splitting intermittently during crystallization, the optical micrograph shown in Figure 5b and recorded for the unprocessed film suggested that there were no signs of crystals. In this latter case, the film surface was covered with

irregular and randomly distributed structures of a few micrometers in size. These are better visualized in Figure 5d as bright, irregular aggregates indicated by the dotted arrows. In between these aggregates, the surface was covered with sub-500 nm structures that exhibited various irregular shapes and were randomly distributed on the surface. One such structure is pointed out in Figure 5f,h by the dotted square shapes, and further magnified in Figure 5j. These structures appeared to be composed of roundish substructures of molecular dimension (32 ± 3 nm in diameter; see the dotted circular green shapes in Figure 5j). The regions in between the sub-500 nm structures were also covered with spherical objects of a molecular diameter (see the dotted circular yellow shapes in Figure 5j). Knowing that PB₁₈₅-*b*-P2VP₁₀₈-*b*-PEO₁₅₄ BCP displays, under specific conditions, a micellar nature [84,85], with micelles that could be exhibiting a total hydrodynamic radius of up to 28.5 nm [84], we cannot exclude the possibility that the as-cast morphology of this BCP system is based on randomly distributed 32 ± 3 nm large micellar objects.

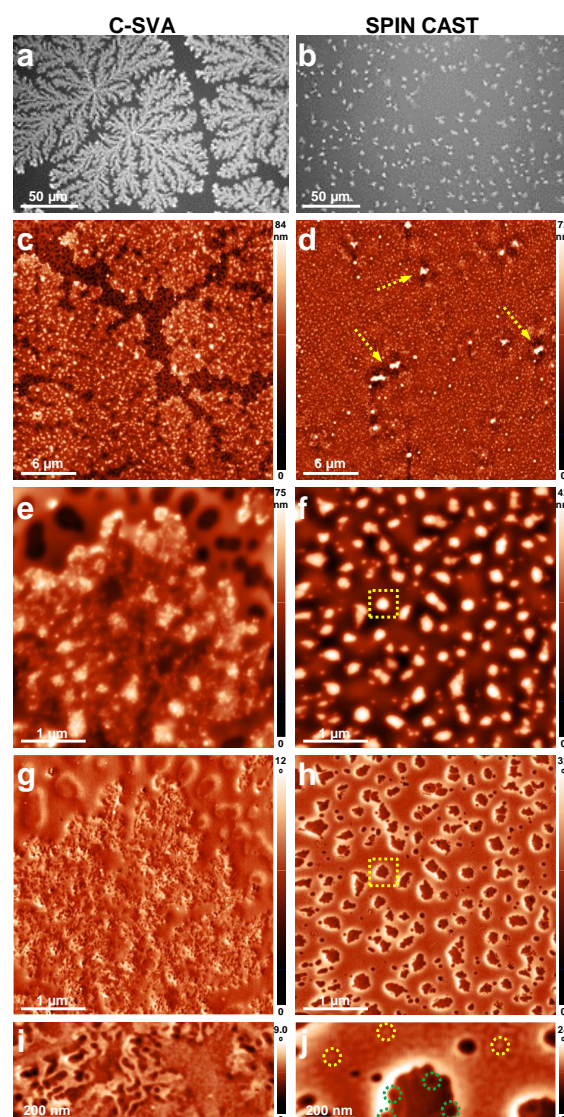


Figure 5. Optical micrographs (a,b) and AFM height (c–f) and phase (g–j) images depicting the surface microstructure observed in a thin film of PB₁₈₅-*b*-P2VP₁₀₈-*b*-PEO₁₅₄ after (a,c,e,g,i) and before (b,d,f,h,j) its exposure to toluene vapors. While height (e) and phase (g) images each represent a zoom-in of a region depicted in (c), images in (f,h) correspond to a zoom-in of a region portrayed in (d). Moreover, micrographs presented in (i,j) are each a zoom-in of the images shown in (g,h), respectively. The purpose of the dotted shapes is for the eye guiding only.

Instead, when the same BCP system was processed by utilizing the C-SVA method, the morphology was composed of crystalline seaweed dendrites of an average height of 29 ± 7 nm (determined by evaluating several cross-sections of the dendrites shown in Figure 5c). As it can be observed in Figure 5e, the dendrites had a rather irregular shape and were surrounded by a rather porous, yet amorphous morphology. Obviously, the latter displayed a darker color in the AFM phase micrograph when compared to the dendritic crystal (Figure 5g). Interestingly, a further magnification of the dendritic area revealed the existence of both folded “stripe”-like and spherical substructures of a few tens of nanometers in lateral dimension (Figure 5i). In conclusion, the comparison between the two morphologies of the PB₁₈₅-*b*-P2VP₁₀₈-*b*-PEO₁₅₄ film obtained before and after its exposure to toluene vapors, revealed again that the crystallization process was induced only in the diluted quasi-2D “film-solution” regime when the C-SVA method was utilized.

Finally, in order to compare the resulting crystalline structures when they are also generated during the spin-casting process, we have massively increased the crystalline PEO block within the BCP system (the ratio between the number of ethylene oxide monomers and the number of total butadiene and 2-vinylpyridine monomers was increased to more than 1.16; in this case the PEO block was expected to be less obstructed by the other two constituent blocks when undergoing crystallization). In Figure 6 we compare a film of PB₃₄₅-*b*-P2VP₂₅₂-*b*-PEO₆₉₇, after and before being processed using the C-SVA method. When the BCP system contained 697 ethylene oxide monomer units, the crystallization process was spotted right after the spin-casting procedure. In this case, the BCP film exhibited a uniform morphology fully covered with densely packed dendritic crystalline structures (23 ± 5 nm in height; Figure 6b,d). Similarly, the film that was processed with the C-SVA method also displayed a surface covered with dendritic crystalline structures, but of a height about 33 ± 7 nm (Figure 6a,c; note here that the dendritic structures formed during the initial spin casting process were dissolved during the exposure of the film to toluene vapors in the “film-solution” configuration and then re-crystallized). In this latter case, some “empty” regions, most probably depleted of chain molecules by the crystallization process, were observed in between the dendrites. Clearly, the dendrites grown in the C-SVA processed film were larger than those grown in the as-spin-cast film (compare Figure 6c with Figure 6d). Moreover, the former dendrites were visibly covered with various polymer decorations of an average height of 20 ± 5 nm (Figure 6e,g). This was not the case for the as-spin-cast dendrites, which only displayed a rather uniform surface (Figure 6f). Interestingly, the decorations were composed of spherical substructures that had an average diameter ranging from ~30 nm to ~55 nm (Figure 6g) and displayed a rather soft texture (as inferred from the AFM phase micrograph shown in Figure 6i). These spherical structures failed to develop during the spin-casting process (Figure 6h,j). In conclusion, when dealing with BCPs composed of rather long crystalline PEO blocks, the crystallization process occurred both after the spin casting and after the C-SVA processing. Nonetheless, only in the latter case were the crystalline dendrites larger, better defined, and displaying decorations composed of spherical soft structures of molecular dimensions.

Similar results to those reported in Figure 6 were also obtained for the PB₆₆-*b*-P2VP₆₉-*b*-PEO₃₅₆ triblock copolymer. Although composed of a shorter PEO block that contained only 356 monomer units, this BCP also exhibited crystalline structures in both C-SVA processed and unprocessed films (Figure 7). Nonetheless, in this case the ratio between the number of ethylene oxide monomers and the number of total butadiene and 2-vinylpyridine monomers was more than 2.63, as the PB and P2VP blocks were reduced to only 66 and 69 monomers, respectively. Therefore, there was not much obstruction of the crystallization process that could have been exerted by the latter two PB and P2VP blocks. Moreover, the fine substructures that can be seen in Figure 7i,j and that form the dendritic crystals shown in Figure 7a,b, are displaying a rather lamellar appearance with lateral dimensions of 18 ± 3 nm in width. Thus, these substructures are not spherical as those observed in Figure 6i,j for the BCP containing a much longer PEO block.

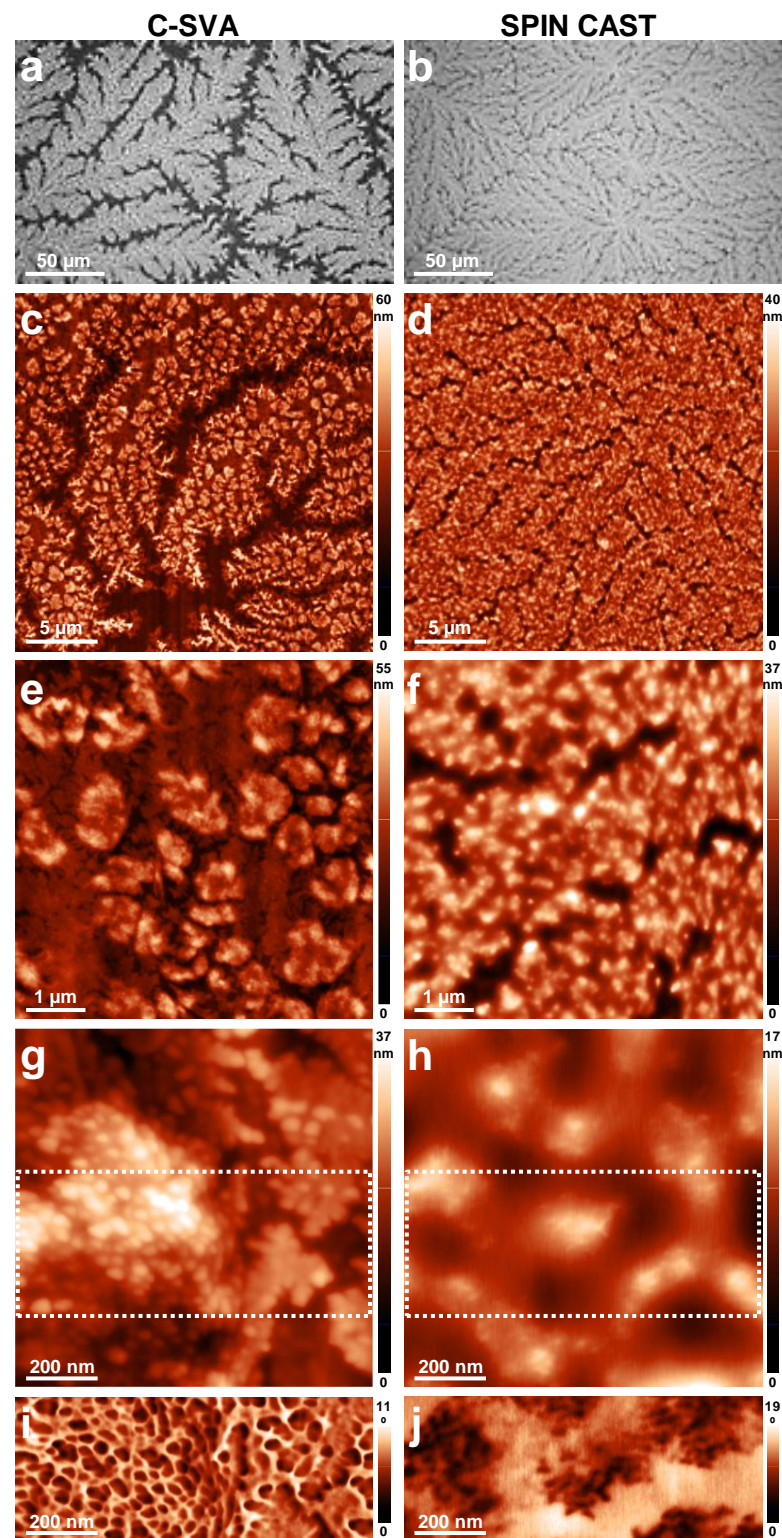


Figure 6. Optical micrographs (a,b) and AFM height (c–h) and phase (i,j) images depicting the surface microstructure observed in a thin film of $PB_{348}\text{-}b\text{-}P2VP_{252}\text{-}b\text{-}PEO_{697}$ after (a,c,e,g,i) and before (b,d,f,h,j) its exposure to toluene vapors in a confined sample chamber. Height images in (e,f) each represent a zoom-in of regions depicted in (c,d), respectively. Similarly, the height images in (g,h) each correspond to a zoom-in of regions portrayed in (e,f), respectively. Moreover, phase images shown in (I,j) are each a zoom-in corresponding to the regions delimited by dotted shapes in (g,h), respectively.

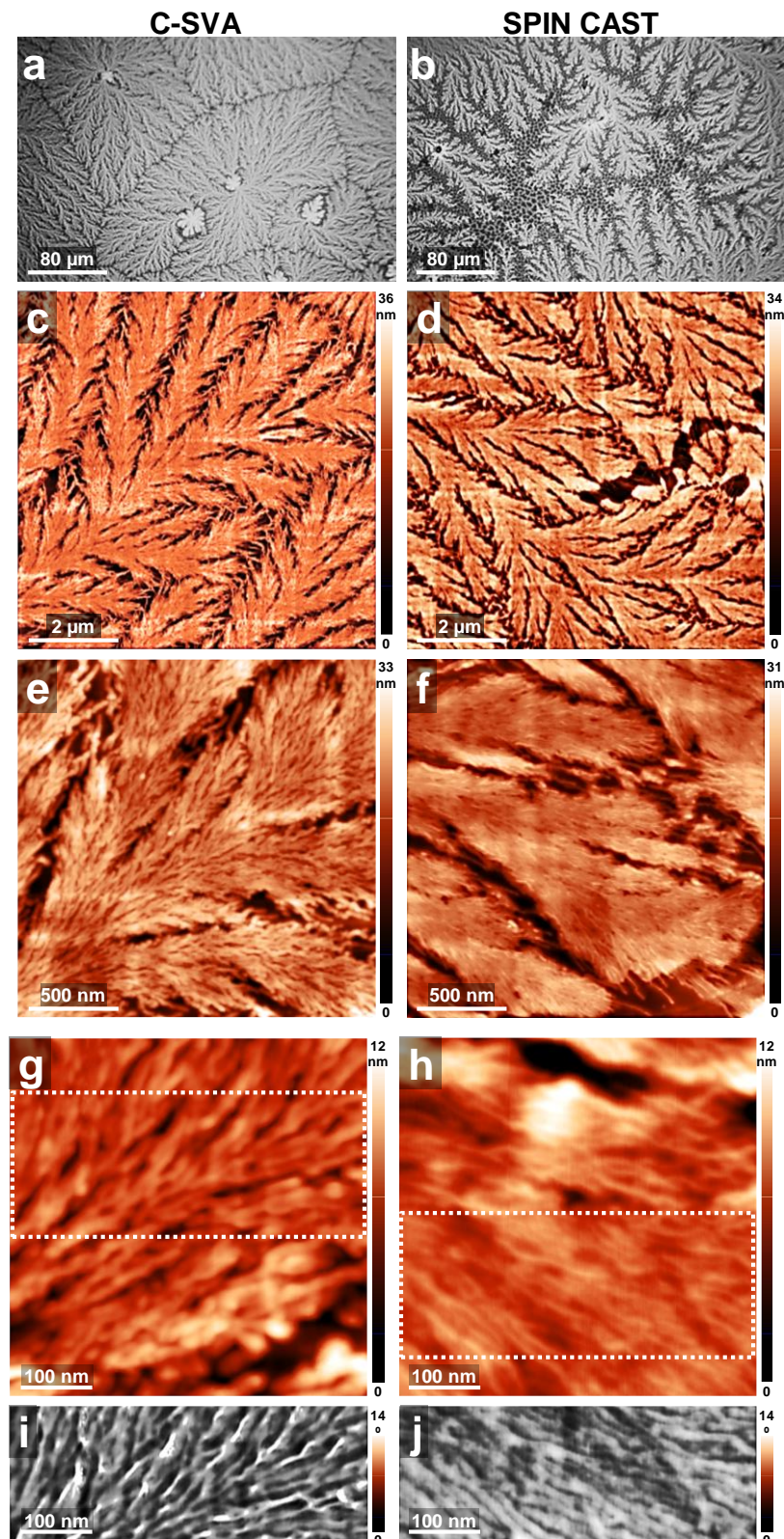


Figure 7. Optical micrographs (**a,b**) and AFM height (**c–h**) and phase (**i,j**) images depicting the surface microstructure observed in a thin film of $\text{PB}_{66}\text{-}b\text{-P2VP}_{69}\text{-}b\text{-PEO}_{356}$ after (**a,c,e,g,i**) and before (**b,d,f,h,j**) its rich-swelling in toluene vapors. Height images in (**e,f**) each represent a zoom-in of regions depicted in (**c,d**), respectively. Similarly, the height images in (**g,h**) each correspond to a zoom-in of regions portrayed in (**e,f**), respectively. Moreover, phase micrographs shown in (**i,j**) are each a zoom-in corresponding to the regions delimited by dotted shapes in (**g,h**), respectively.

4. Conclusions

We have used a polymer processing approach based on solvent vapor annealing in a space-confined environment in order to induce crystallization in thin films of PB-*b*-P2VP-*b*-PEO triblock copolymers that contained a rather short crystalline PEO and which would not crystallize otherwise. Indeed, the obtained optical microscopy and AFM results have shown that the PB-*b*-P2VP-*b*-PEO films based on short PEO blocks (i.e., 104–154 monomer units) that were well hindered by the other two constituent blocks led to crystals of (seaweed) dendritic morphology only following their generous swelling in solvent vapors. As expected, the BCP films based on a much longer PEO crystalline block (i.e., 356–697 monomers) that were less hindered by the other two constituent blocks underwent crystallization inclusively under normal spin-casting conditions.

Author Contributions: Conceptualization, I.B. (Iulia Babutan), O.T.-B., L.I.A. and I.B. (Ioan Botiz); Methodology, O.T.-B., L.I.A., A.V. and I.B. (Ioan Botiz); Formal analysis, I.B. (Iulia Babutan), O.T.-B. and I.B. (Ioan Botiz); Investigation, I.B. (Iulia Babutan) and I.B. (Ioan Botiz); Writing—original draft, I.B. (Iulia Babutan); Writing—review & editing, L.I.A., A.V. and I.B. (Ioan Botiz); Supervision, I.B. (Ioan Botiz); Project administration, A.V.; Funding acquisition, A.V. All authors have read and agreed to the published version of the manuscript.

Funding: A.V. and I.B. acknowledge the financial support of the Romanian National Authority for Scientific Research and Innovation, CNCS-UEFISCDI, project no. PN-III-P1-1.1-TE-2021-0388.

Institutional Review Board Statement: Not applicable.

Informed Consent Statement: Not applicable.

Data Availability Statement: The data presented in this study are available on request from the corresponding author.

Conflicts of Interest: The authors declare no conflict of interest.

References

1. Ronca, S. Chapter 10—Polyethylene. In *Brydson's Plastics Materials*, 8th ed.; Gilbert, M., Ed.; Butterworth-Heinemann: Oxford, UK; pp. 247–278, ISBN 978-0-323-35824-8.
2. Babutan, I.; Lucaci, A.-D.; Botiz, I. Antimicrobial Polymeric Structures Assembled on Surfaces. *Polymers* **2021**, *13*, 1552. [[CrossRef](#)] [[PubMed](#)]
3. Moohan, J.; Stewart, S.A.; Espinosa, E.; Rosal, A.; Rodríguez, A.; Larrañeta, E.; Donnelly, R.F.; Domínguez-Robles, J. Cellulose Nanofibers and Other Biopolymers for Biomedical Applications. A Review. *Appl. Sci.* **2020**, *10*, 65. [[CrossRef](#)]
4. Pattanashetti, N.A.; Heggannavar, G.B.; Kariduraganavar, M.Y. Smart Biopolymers and Their Biomedical Applications. *Procedia Manuf.* **2017**, *12*, 263–279. [[CrossRef](#)]
5. Smith, M.; Kar-Narayan, S. Piezoelectric Polymers: Theory, Challenges and Opportunities. *Int. Mater. Rev.* **2022**, *67*, 65–88. [[CrossRef](#)]
6. Yao, H.; Fan, Z.; Cheng, H.; Guan, X.; Wang, C.; Sun, K.; Ouyang, J. Recent Development of Thermoelectric Polymers and Composites. *Macromol. Rapid Commun.* **2018**, *39*, 1700727. [[CrossRef](#)]
7. Tarcan, R.; Handrea-Dragan, M.; Leordean, C.-I.; Cioban, R.C.; Kiss, G.-Z.; Zaharie-Butucel, D.; Farcau, C.; Vulpoi, A.; Simon, S.; Botiz, I. Development of Polymethylmethacrylate/Reduced Graphene Oxide Composite Films as Thermal Interface Materials. *J. Appl. Polym. Sci.* **2022**, *139*, e53238. [[CrossRef](#)]
8. Foster, D.P.; Majumdar, D. Critical Behavior of Magnetic Polymers in Two and Three Dimensions. *Phys. Rev. E* **2021**, *104*, 024122. [[CrossRef](#)]
9. Botiz, I.; Durbin, M.M.; Stingelin, N. Providing a Window into the Phase Behavior of Semiconducting Polymers. *Macromolecules* **2021**, *54*, 5304–5320. [[CrossRef](#)]
10. Botiz, I.; Astilean, S.; Stingelin, N. Altering the Emission Properties of Conjugated Polymers. *Polym. Int.* **2016**, *65*, 157–163. [[CrossRef](#)]
11. Nguyen, H.V.-T.; Jiang, Y.; Mohapatra, S.; Wang, W.; Barnes, J.C.; Oldenhuis, N.J.; Chen, K.K.; Axelrod, S.; Huang, Z.; Chen, Q.; et al. Bottlebrush Polymers with Flexible Enantiomeric Side Chains Display Differential Biological Properties. *Nat. Chem.* **2022**, *14*, 85–93. [[CrossRef](#)]
12. Song, X.; Gan, B.; Qi, S.; Guo, H.; Tang, C.Y.; Zhou, Y.; Gao, C. Intrinsic Nanoscale Structure of Thin Film Composite Polyamide Membranes: Connectivity, Defects, and Structure–Property Correlation. *Environ. Sci. Technol.* **2020**, *54*, 3559–3569. [[CrossRef](#)] [[PubMed](#)]

13. Shi, Y.; Guo, H.; Qin, M.; Wang, Y.; Zhao, J.; Sun, H.; Wang, H.; Wang, Y.; Zhou, X.; Facchetti, A.; et al. Imide-Functionalized Thiazole-Based Polymer Semiconductors: Synthesis, Structure–Property Correlations, Charge Carrier Polarity, and Thin-Film Transistor Performance. *Chem. Mater.* **2018**, *30*, 7988–8001. [[CrossRef](#)]
14. Botiz, I. Prominent Processing Techniques to Manipulate Semiconducting Polymer Microstructure. *J. Mater. Chem. C* **2023**, *11*, 364–405. [[CrossRef](#)]
15. Botiz, I.; Freyberg, P.; Leordean, C.; Gabudean, A.-M.; Astilean, S.; Yang, A.C.-M.; Stingelin, N. Emission Properties of MEH-PPV in Thin Films Simultaneously Illuminated and Annealed at Different Temperatures. *Synth. Met.* **2015**, *199*, 33–36. [[CrossRef](#)]
16. Peng, Z.; Stingelin, N.; Ade, H.; Michels, J.J. A Materials Physics Perspective on Structure-Processing-Function Relations in Blends of Organic Semiconductors. *Nat. Rev. Mater.* **2023**, 1–17. [[CrossRef](#)]
17. Dimov, I.B.; Moser, M.; Malliaras, G.G.; McCulloch, I. Semiconducting Polymers for Neural Applications. *Chem. Rev.* **2022**, *122*, 4356–4396. [[CrossRef](#)] [[PubMed](#)]
18. de Leon, A.C.C.; da Silva, Í.G.M.; Pangilinan, K.D.; Chen, Q.; Caldon, E.B.; Advincula, R.C. High Performance Polymers for Oil and Gas Applications. *React. Funct. Polym.* **2021**, *162*, 104878. [[CrossRef](#)]
19. Pham, Q.-T.; Chern, C.-S. Applications of Polymers in Lithium-Ion Batteries with Enhanced Safety and Cycle Life. *J. Polym. Res.* **2022**, *29*, 124. [[CrossRef](#)]
20. Yarali, E.; Baniasadi, M.; Zolfagharian, A.; Chavoshi, M.; Arefi, F.; Hossain, M.; Bastola, A.; Ansari, M.; Foyouzat, A.; Dabbagh, A.; et al. Magneto-/ Electro-responsive Polymers toward Manufacturing, Characterization, and Biomedical/Soft Robotic Applications. *Appl. Mater. Today* **2022**, *26*, 101306. [[CrossRef](#)]
21. Angel, N.; Li, S.; Yan, F.; Kong, L. Recent Advances in Electrospinning of Nanofibers from Bio-Based Carbohydrate Polymers and Their Applications. *Trends Food Sci. Technol.* **2022**, *120*, 308–324. [[CrossRef](#)]
22. He, Y.; Kukhta, N.A.; Marks, A.; Luscombe, C.K. The Effect of Side Chain Engineering on Conjugated Polymers in Organic Electrochemical Transistors for Bioelectronic Applications. *J. Mater. Chem. C* **2022**, *10*, 2314–2332. [[CrossRef](#)] [[PubMed](#)]
23. Handrea-Dragan, M.; Botiz, I. Multifunctional Structured Platforms: From Patterning of Polymer-Based Films to Their Subsequent Filling with Various Nanomaterials. *Polymers* **2021**, *13*, 445. [[CrossRef](#)] [[PubMed](#)]
24. Mohanty, A.K.; Wu, F.; Mincheva, R.; Hakkarainen, M.; Raquez, J.-M.; Mielewski, D.F.; Narayan, R.; Netravali, A.N.; Misra, M. Sustainable Polymers. *Nat. Rev. Methods Primers* **2022**, *2*, 1–27. [[CrossRef](#)]
25. Chohan, J.S.; Boparai, K.S.; Singh, R.; Hashmi, M.S.J. Manufacturing Techniques and Applications of Polymer Matrix Composites: A Brief Review. *Adv. Mater. Process. Technol.* **2022**, *8*, 884–894. [[CrossRef](#)]
26. Sun, C.; Zhu, C.; Meng, L.; Li, Y. Quinoxaline-Based D–A Copolymers for the Applications as Polymer Donor and Hole Transport Material in Polymer/Perovskite Solar Cells. *Adv. Mater.* **2022**, *34*, 2104161. [[CrossRef](#)]
27. Ritsema van Eck, G.C.; Chiappisi, L.; de Beer, S. Fundamentals and Applications of Polymer Brushes in Air. *ACS Appl. Polym. Mater.* **2022**, *4*, 3062–3087. [[CrossRef](#)]
28. Kirillova, A.; Yeazel, T.R.; Asheghali, D.; Petersen, S.R.; Dort, S.; Gall, K.; Becker, M.L. Fabrication of Biomedical Scaffolds Using Biodegradable Polymers. *Chem. Rev.* **2021**, *121*, 11238–11304. [[CrossRef](#)] [[PubMed](#)]
29. Fischer, F.S.U.; Tremel, K.; Saur, A.-K.; Link, S.; Kayunkid, N.; Brinkmann, M.; Herrero-Carvajal, D.; Navarrete, J.T.L.; Delgado, M.C.R.; Ludwigs, S. Influence of Processing Solvents on Optical Properties and Morphology of a Semicrystalline Low Bandgap Polymer in the Neutral and Charged States. *Macromolecules* **2013**, *46*, 4924–4931. [[CrossRef](#)]
30. Baklar, M.A.; Koch, F.; Kumar, A.; Buchaca Domingo, E.; Campoy-Quiles, M.; Feldman, K.; Yu, L.; Wöbkenberg, P.; Ball, J.; Wilson, R.M.; et al. Solid-State Processing of Organic Semiconductors. *Adv. Mater.* **2010**, *22*, 3942–3947. [[CrossRef](#)]
31. Botiz, I.; Codescu, M.-A.; Farcau, C.; Leordean, C.; Astilean, S.; Silva, C.; Stingelin, N. Convective Self-Assembly of π -Conjugated Oligomers and Polymers. *J. Mater. Chem. C* **2017**, *5*, 2513–2518. [[CrossRef](#)]
32. Peterson, G.W.; Lee, D.T.; Barton, H.F.; Epps, T.H.; Parsons, G.N. Fibre-Based Composites from the Integration of Metal–Organic Frameworks and Polymers. *Nat. Rev. Mater.* **2021**, *6*, 605–621. [[CrossRef](#)]
33. Chowdhury, M.; Sajjad, M.T.; Savikhin, V.; Hergué, N.; Sutija, K.B.; Oosterhout, S.D.; Toney, M.F.; Dubois, P.; Ruseckas, A.; Samuel, I.D.W. Tuning Crystalline Ordering by Annealing and Additives to Study Its Effect on Exciton Diffusion in a Polyalkylthiophene Copolymer. *Phys. Chem. Chem. Phys.* **2017**, *19*, 12441–12451. [[CrossRef](#)] [[PubMed](#)]
34. Todor-Boer, O.; Petrovai, I.; Tarcan, R.; Vulpoi, A.; David, L.; Astilean, S.; Botiz, I. Enhancing Photoluminescence Quenching in Donor–Acceptor PCE11:PPCBMB Films through the Optimization of Film Microstructure. *Nanomaterials* **2019**, *9*, 1757. [[CrossRef](#)] [[PubMed](#)]
35. Li, Q.-Y.; Yao, Z.-F.; Lu, Y.; Zhang, S.; Ahmad, Z.; Wang, J.-Y.; Gu, X.; Pei, J. Achieving High Alignment of Conjugated Polymers by Controlled Dip-Coating. *Adv. Electron. Mater.* **2020**, *6*, 2000080. [[CrossRef](#)]
36. Xiao, M.; Kang, B.; Lee, S.B.; Perdigão, L.M.A.; Luci, A.; Warr, D.A.; Senanayak, S.P.; Nikolka, M.; Statz, M.; Wu, Y.; et al. Anisotropy of Charge Transport in a Uniaxially Aligned Fused Electron-Deficient Polymer Processed by Solution Shear Coating. *Adv. Mater.* **2020**, *32*, 2000063. [[CrossRef](#)]
37. Basu, A.; Niazi, M.R.; Scaccabarozzi, A.D.; Faber, H.; Fei, Z.; Anjum, D.H.; Paterson, A.F.; Boltalina, O.; Heeney, M.; Anthopoulos, T.D. Impact of P-Type Doping on Charge Transport in Blade-Coated Small-Molecule:Polymer Blend Transistors. *J. Mater. Chem. C* **2020**, *8*, 15368–15376. [[CrossRef](#)]
38. Grozev, N.; Botiz, I.; Reiter, G. Morphological Instabilities of Polymer Crystals. *Eur. Phys. J. E* **2008**, *27*, 63–71. [[CrossRef](#)]

39. Botiz, I.; Grozev, N.; Schlaad, H.; Reiter, G. The Influence of Protic Non-Solvents Present in the Environment on Structure Formation of Poly(γ -Benzyl-L-Glutamate in Organic Solvents. *Soft Matter* **2008**, *4*, 993–1002. [[CrossRef](#)]
40. Darko, C.; Botiz, I.; Reiter, G.; Breiby, D.W.; Andreasen, J.W.; Roth, S.V.; Smilgies, D.M.; Metwalli, E.; Papadakis, C.M. Crystallization in Diblock Copolymer Thin Films at Different Degrees of Supercooling. *Phys. Rev. E* **2009**, *79*, 041802. [[CrossRef](#)]
41. Jahanshahi, K.; Botiz, I.; Reiter, R.; Thomann, R.; Heck, B.; Shokri, R.; Stille, W.; Reiter, G. Crystallization of Poly(γ -Benzyl L-Glutamate) in Thin Film Solutions: Structure and Pattern Formation. *Macromolecules* **2013**, *46*, 1470–1476. [[CrossRef](#)]
42. Jahanshahi, K.; Botiz, I.; Reiter, R.; Scherer, H.; Reiter, G. Reversible Nucleation, Growth, and Dissolution of Poly(γ -Benzyl L-Glutamate) Hexagonal Columnar Liquid Crystals by Addition and Removal of a Nonsolvent. *Cryst. Growth Des.* **2013**, *13*, 4490–4494. [[CrossRef](#)]
43. Singh, M.; Agrawal, A.; Wu, W.; Masud, A.; Armijo, E.; Gonzalez, D.; Zhou, S.; Terlier, T.; Zhu, C.; Strzalka, J.; et al. Soft-Shear-Aligned Vertically Oriented Lamellar Block Copolymers for Template-Free Sub-10 Nm Patterning and Hybrid Nanostructures. *ACS Appl. Mater. Interfaces* **2022**, *14*, 12824–12835. [[CrossRef](#)] [[PubMed](#)]
44. Zhang, Q.; Weber, C.; Schubert, U.S.; Hoogenboom, R. Thermoresponsive Polymers with Lower Critical Solution Temperature: From Fundamental Aspects and Measuring Techniques to Recommended Turbidimetry Conditions. *Mater. Horiz.* **2017**, *4*, 109–116. [[CrossRef](#)]
45. Macedo, A.S.; Carvalho, E.O.; Cardoso, V.F.; Correia, D.M.; Tubio, C.R.; Fidalgo-Marijuan, A.; Botelho, G.; Lanceros-Méndez, S. Tailoring Electroactive Poly(Vinylidene Fluoride-co-Trifluoroethylene) Microspheres by a Nanoprecipitation Method. *Mater. Lett.* **2020**, *261*, 127018. [[CrossRef](#)]
46. Lin, X.; Liu, R.; Ding, C.; Deng, J.; Guo, Y.; Long, S.; Li, L.; Li, M. Modulation of Microstructure and Charge Transport in Polymer Monolayer Transistors by Solution Aging. *Chin. J. Chem.* **2021**, *39*, 3079–3084. [[CrossRef](#)]
47. Khalil, Y.; Hopkinson, N.; Kowalski, A.; Fairclough, J.P.A. Characterisation of UHMWPE Polymer Powder for Laser Sintering. *Materials* **2019**, *12*, 3496. [[CrossRef](#)]
48. Jana, A.; Selvaraj, S.; Subramani, K. A Novel Technique for the Development of Acetabular Cup by Cold Isostatic Compaction and Sintering of UHMWPE Powder with Optimized Processing Parameters. *Polym. Eng. Sci.* **2021**, *61*, 2536–2556. [[CrossRef](#)]
49. Khan, A.L.T.; Sreearunothai, P.; Herz, L.M.; Banach, M.J.; Köhler, A. Morphology-Dependent Energy Transfer within Polyfluorene Thin Films. *Phys. Rev. B* **2004**, *69*, 085201. [[CrossRef](#)]
50. Danesh, C.D.; Starkweather, N.S.; Zhang, S. In Situ Study of Dynamic Conformational Transitions of a Water-Soluble Poly(3-Hexylthiophene) Derivative by Surfactant Complexation. *J. Phys. Chem. B* **2012**, *116*, 12887–12894. [[CrossRef](#)]
51. Adachi, T.; Tong, L.; Kuwabara, J.; Kanbara, T.; Saeki, A.; Seki, S.; Yamamoto, Y. Spherical Assemblies from π -Conjugated Alternating Copolymers: Toward Optoelectronic Colloidal Crystals. *J. Am. Chem. Soc.* **2013**, *135*, 870–876. [[CrossRef](#)]
52. Guha, S.; Chandrasekhar, M.; Scherf, U.; Knaapila, M. Tuning Structural and Optical Properties of Blue-Emitting Polymeric Semiconductors. *Phys. Status Solidi B* **2011**, *248*, 1083–1090. [[CrossRef](#)]
53. Tung, K.-P.; Chen, C.-C.; Lee, P.; Liu, Y.-W.; Hong, T.-M.; Hwang, K.C.; Hsu, J.H.; White, J.D.; Yang, A.C.-M. Large Enhancements in Optoelectronic Efficiencies of Nano-Plastically Stressed Conjugated Polymer Strands. *ACS Nano* **2011**, *5*, 7296–7302. [[CrossRef](#)] [[PubMed](#)]
54. Loo, Y.L.; Register, R.A.; Ryan, A.J. Modes of Crystallization in Block Copolymer Microdomains: Breakout, Templated, and Confined. *Macromolecules* **2002**, *35*, 2365–2374. [[CrossRef](#)]
55. Bao, J.; Dong, X.; Chen, S.; Lu, W.; Zhang, X.; Chen, W. Confined Crystallization, Melting Behavior and Morphology in PEG-b-PLA Diblock Copolymers: Amorphous versus Crystalline PLA. *J. Polym. Sci.* **2020**, *58*, 455–465. [[CrossRef](#)]
56. MacFarlane, L.R.; Shaikh, H.; Garcia-Hernandez, J.D.; Vespa, M.; Fukui, T.; Manners, I. Functional Nanoparticles through π -Conjugated Polymer Self-Assembly. *Nat. Rev. Mater.* **2021**, *6*, 7–26. [[CrossRef](#)]
57. Stevens, C.A.; Kaur, K.; Klok, H.-A. Self-Assembly of Protein-Polymer Conjugates for Drug Delivery. *Adv. Drug Deliv. Rev.* **2021**, *174*, 447–460. [[CrossRef](#)]
58. Scanga, R.A.; Reuther, J.F. Helical Polymer Self-Assembly and Chiral Nanostructure Formation. *Polym. Chem.* **2021**, *12*, 1857–1897. [[CrossRef](#)]
59. Kos, P.I.; Ivanov, V.A.; Chertovich, A.V. Crystallization of Semiflexible Polymers in Melts and Solutions. *Soft Matter* **2021**, *17*, 2392–2403. [[CrossRef](#)]
60. Jin, F.; Yuan, S.; Wang, S.; Zhang, Y.; Zheng, Y.; Hong, Y.; Miyoshi, T. Polymer Chains Fold Prior to Crystallization. *ACS Macro Lett.* **2022**, *11*, 284–288. [[CrossRef](#)]
61. Sheng, J.; Chen, W.; Cui, K.; Li, L. Polymer Crystallization under External Flow. *Rep. Prog. Phys.* **2022**, *85*, 036601. [[CrossRef](#)]
62. Xu, W.; Li, X.; Zheng, Y.; Yuan, W.; Zhou, J.; Yu, C.; Bao, Y.; Shan, G.; Pan, P. Hierarchical Ordering and Multilayer Structure of Poly(ϵ -Caprolactone) End-Functionalized by a Liquid Crystalline Unit: Role of Polymer Crystallization. *Polym. Chem.* **2021**, *12*, 4175–4183. [[CrossRef](#)]
63. Hamley, I.W. Crystallization in Block Copolymers. In *Interfaces Crystallization Viscoelasticity*; Springer: Berlin/Heidelberg, Germany, 1999; pp. 113–137. ISBN 978-3-540-48836-1.
64. Castillo, R.V.; Müller, A.J. Crystallization and Morphology of Biodegradable or Biostable Single and Double Crystalline Block Copolymers. *Prog. Polym. Sci.* **2009**, *34*, 516–560. [[CrossRef](#)]

65. Le, T.P.; Smith, B.H.; Lee, Y.; Litofsky, J.H.; Aplan, M.P.; Kuei, B.; Zhu, C.; Wang, C.; Hexemer, A.; Gomez, E.D. Enhancing Optoelectronic Properties of Conjugated Block Copolymers through Crystallization of Both Blocks. *Macromolecules* **2020**, *53*, 1967–1976. [[CrossRef](#)]
66. He, Y.; Eloi, J.-C.; Harniman, R.L.; Richardson, R.M.; Whittell, G.R.; Mathers, R.T.; Dove, A.P.; O'Reilly, R.K.; Manners, I. Uniform Biodegradable Fiber-Like Micelles and Block Comicelles via “Living” Crystallization-Driven Self-Assembly of Poly(l-Lactide) Block Copolymers: The Importance of Reducing Unimer Self-Nucleation via Hydrogen Bond Disruption. *J. Am. Chem. Soc.* **2019**, *141*, 19088–19098. [[CrossRef](#)] [[PubMed](#)]
67. Hamley, I.W. Block Copolymers. In *Encyclopedia of Polymer Science and Technology*; John Wiley & Sons, Ltd.: Hoboken, NJ, USA, 2002; Volume 1, pp. 457–482.
68. Xiong, S.; Li, D.; Hur, S.-M.; Craig, G.S.W.; Arges, C.G.; Qu, X.-P.; Nealey, P.F. The Solvent Distribution Effect on the Self-Assembly of Symmetric Triblock Copolymers during Solvent Vapor Annealing. *Macromolecules* **2018**, *51*, 7145–7151. [[CrossRef](#)]
69. Shi, L.-Y.; Yin, C.; Zhou, B.; Xia, W.; Weng, L.; Ross, C.A. Annealing Process Dependence of the Self-Assembly of Rod–Coil Block Copolymer Thin Films. *Macromolecules* **2021**, *54*, 1657–1664. [[CrossRef](#)]
70. Ginige, G.; Song, Y.; Olsen, B.C.; Lubner, E.J.; Yavuz, C.T.; Buriak, J.M. Solvent Vapor Annealing, Defect Analysis, and Optimization of Self-Assembly of Block Copolymers Using Machine Learning Approaches. *ACS Appl. Mater. Interfaces* **2021**, *13*, 28639–28649. [[CrossRef](#)] [[PubMed](#)]
71. Atanase, L.I.; Lerch, J.-P.; Caprarescu, S.; Iurciuc, C.E.; Riess, G. Micellization of PH-Sensitive Poly(Butadiene)-Block-Poly(2-Vinylpyridine)-Block-Poly(Ethylene Oxide) Triblock Copolymers: Complex Formation with Anionic Surfactants. *J. Appl. Polym. Sci.* **2017**, *134*, 45313. [[CrossRef](#)]
72. Zhao, W.; Su, Y.; Müller, A.J.; Gao, X.; Wang, D. Direct Relationship Between Interfacial Microstructure and Confined Crystallization in Poly(Ethylene Oxide)/Silica Composites: The Study of Polymer Molecular Weight Effects. *J. Polym. Sci. B Polym. Phys.* **2017**, *55*, 1608–1616. [[CrossRef](#)]
73. Babutan, I.; Todor-Boer, O.; Atanase, L.I.; Vulpoi, A.; Simon, S.; Botiz, I. Self-Assembly of Block Copolymers on Surfaces Exposed to Space-Confined Solvent Vapor Annealing. *Polymer* **2023**, *273*, 125881. [[CrossRef](#)]
74. Babutan, I.; Todor-Boer, O.; Atanase, L.I.; Vulpoi, A.; Botiz, I. Self-Assembly of Block Copolymers in Thin Films Swollen-Rich in Solvent Vapors. *Polymers* **2023**, *15*, 1900. [[CrossRef](#)] [[PubMed](#)]
75. Reiter, G.; Botiz, I.; Graveleau, L.; Grozev, N.; Albrecht, K.; Mourran, A.; Möller, M. Morphologies of Polymer Crystals in Thin Films. In *Lecture Notes in Physics: Progress in Understanding of Polymer Crystallization*; Reiter, G., Strobl, G.R., Eds.; Springer: Berlin/Heidelberg, Germany, 2007; Volume 714, pp. 179–200. [[CrossRef](#)]
76. Soum, A.; Fontanille, M.; Sigwalt, P. Anionic Polymerization of 2-Vinylpyridine Initiated by Symmetrical Organomagnesium Compounds in Tetrahydrofuran. *J. Polym. Sci. Polym. Chem. Ed.* **1977**, *15*, 659–673. [[CrossRef](#)]
77. Atanase, L.I.; Riess, G. Stabilization of Non-Aqueous Emulsions by Poly(2-Vinylpyridine)-b-Poly(Butadiene) Block Copolymers. *Colloids Surf. A Physicochem. Eng. Asp.* **2014**, *458*, 19–24. [[CrossRef](#)]
78. Botiz, I.; Schlaad, H.; Reiter, G. Processes of Ordered Structure Formation in Polypeptide Thin Film Solutions. In *Self Organized Nanostructures of Amphiphilic Block Copolymers II*; Springer: Berlin/Heidelberg, Germany, 2011; Volume 242, pp. 117–149.
79. Kovacs, A.J.; Straupe, C.; Gonthier, A. Isothermal Growth, Thickening, and Melting of Poly(ethylene Oxide) Single Crystals in the Bulk. II. *J. Polym. Sci. Polym. Symp.* **1977**, *59*, 31–54. [[CrossRef](#)]
80. Lysenko, E.A.; Bronich, T.K.; Slonkina, E.V.; Eisenberg, A.; Kabanov, V.A.; Kabanov, A.V. Block Ionomer Complexes with Polystyrene Core-Forming Block in Selective Solvents of Various Polarities. 2. Solution Behavior and Self-Assembly in Nonpolar Solvents. *Macromolecules* **2002**, *35*, 6344–6350. [[CrossRef](#)]
81. Changez, M.; Kang, N.-G.; Koh, H.-D.; Lee, J.-S. Effect of Solvent Composition on Transformation of Micelles to Vesicles of Rod–Coil Poly(n-Hexyl Isocyanate-Block-2-Vinylpyridine) Diblock Copolymers. *Langmuir* **2010**, *26*, 9981–9985. [[CrossRef](#)]
82. Ferreira, V.; Douglas, J.F.; Warren, J.; Karim, A. Growth Pulsations in Symmetric Dendritic Crystallization in Thin Polymer Blend Films. *Phys. Rev. E* **2002**, *65*, 051606. [[CrossRef](#)]
83. Ferreira, V.; Douglas, J.F.; Warren, J.A.; Karim, A. Nonequilibrium Pattern Formation in the Crystallization of Polymer Blend Films. *Phys. Rev. E* **2002**, *65*, 042802. [[CrossRef](#)]
84. Riess, G. Micellization of Block Copolymers. *Prog. Polym. Sci.* **2003**, *28*, 1107–1170. [[CrossRef](#)]
85. Lerch, J.-P. Synthesis and Characterization of Amphiphilic Block- and Graft Terpolymers. Study of Inorganic Dispersions in Aqueous and Non-Aqueous Media. Ph.D. Thesis, University Haute Alsace, Mulhouse, France, 1996.

Disclaimer/Publisher’s Note: The statements, opinions and data contained in all publications are solely those of the individual author(s) and contributor(s) and not of MDPI and/or the editor(s). MDPI and/or the editor(s) disclaim responsibility for any injury to people or property resulting from any ideas, methods, instructions or products referred to in the content.